nature geoscience

SUPPLEMENTARY INFORMATION

DOI: 10.1038/NGEO3002

In the format provided by the authors and unedited.

Large sulfur isotope fractionations in Martian sediments at Gale crater

H. B. Franz, A. C. McAdam, D. W. Ming, C. Freissinet, P. R. Mahaffy, D. L. Eldridge, W. W. Fischer, J. P. Grotzinger, C. H. House, J. A. Hurowitz, S. M. McLennan, S. P. Schwenzer, D. T. Vaniman, P. D. Archer, Jr., S. K. Atreya, P. G. Conrad, J. W. Dottin III, J. L. Eigenbrode, K. A. Farley, D. P. Glavin, S. S. Johnson, C. A. Knudson, R. V. Morris, R. Navarro-González, A. A. Pavlov, R. Plummer, E. B. Rampe, J. C. Stern, A. Steele, R. E. Summons, B. Sutter

This file contains additional discussion relevant to interpretation of sulfur isotope data, extended description of methods, calibration data, supplementary figures and data tables, and additional references.

Geological Context

Gale crater, 154 km in diameter, was formed ~3.8 to 3.6 billion years ago[42,43] during the late Noachian to early Hesperian period of Mars' history[44]. It is situated approximately 5° south of the equator at the Martian dichotomy boundary between ancient, heavily cratered southern highlands and the younger northern plains[45] in an area characterized by fluvial dissection[1]. The crater is dominated by Mt. Sharp, a central mound of sediments ~ 5 km high with a base of interbedded phyllosilicates and sulfates that transitions upward into sulfate-dominated deposits[45]. A moat around Mt. Sharp, exposed by eolian erosion, contains sedimentary surfaces dated by crater counts to 3.3 to 3.1 billion years ago[1]. The sulfur isotopic compositions measured by Curiosity most likely reflect effects of the Martian sulfur cycle that operated during this time

period, with the exception of detrital components that may record earlier processing of sulfur. These sediments, probably sourced from the crater's northern rim and deposited in fluvial, deltaic, and lacustrine environments, are liberally marked by erosion-resistant ridges, sulfate veins, concretions, and hollow nodules indicating post-depositional diagenesis involving sulfur [15,28,46,47].

Samples described here were obtained from two stratigraphic groups, known as the Bradbury Group and the Mount Sharp Group and depicted in the stratigraphic column of Fig. 1[1]. The lowest-lying sediments sampled by Curiosity were those of the Yellowknife Bay formation of the Bradbury Group[48]. Two drilling locations ~3 m apart in the Sheepbed lacustrine mudstone of Yellowknife Bay, designated John Klein (JK) and Cumberland (CB), were selected based on differences in visible diagenetic features, with JK containing more sulfate-rich veins and CB containing more hollow nodules[15,28]. The Windjana (WJ) sample was acquired from thinly cross-bedded fluvial sandstone of the Kimberley formation ~40 m above the Sheepbed mudstone[39]. Five samples of the Murray formation, designated Confidence Hills (CH), Mojave2 (MJ), Telegraph Peak (TP), Buckskin (BK), and Oudam (OU), were drilled from fine-grained laminated mudstone ~20-45 m above Windjana[1]. The Pahrump Hills section from which they were acquired contains pervasive diagenetic features and minerals that suggest an alteration history distinct from that of the Bradbury Group[49]. Stratigraphic relationships between the Murray formation and Bradbury Group are not entirely clear, but it is likely either that the Bradbury Group and Murray formations are interfingered and syndepositional or that the Bradbury Group is younger and was deposited unconformably atop the Murray formation[1]. Finally, Greenhorn (GH) and Big Sky (BY), from elevation similar to that of OU, represent

altered and unaltered samples of cross-bedded eolian sandstone from the Stimson formation that overlies the Murray formation[50].

Sample Mineralogy

Analyses by the Chemistry and Mineralogy Instrument (CheMin) show that JK and CB samples from the Sheepbed mudstone are comprised predominantly of basaltic silicate minerals (including plagioclase, several pyroxenes, and small amounts of olivine) and Fe-smectites (~20 wt %). They also possess ~4 wt % magnetite, minor akaganeite (1.1 wt % in JK, 1.7 wt % in CB), 1 wt % pyrrhotite, and the Ca sulfates anhydrite (2.6 wt % in JK, 0.8 wt % in CB) and bassanite (1.0 wt % in JK, 0.7 wt % in CB)[14]. These samples also had significant amounts of sulfur-rich amorphous material (~30 wt%)[14,51]. Many aspects of the mineral assemblage, such as the presence of magnetite and smectite clay minerals and lack of Fe-sulfates, indicate alteration under circumneutral pH conditions, although a small amount of acidic alteration is indicated by the presence of akaganeite. We hypothesize that the pyrrhotite in both samples was largely formed from diagenetic fluids associated with impact hydrothermalism, but that the difference in sulfur isotopic composition of these sulfides in CB versus JK may result from later introduction of sulfur bearing a more enriched composition. This same fluid may have also partially oxidized some preexisting sulfide in the samples. Several contextual observations support the idea that localized interactions with different diagenetic fluids over time could explain the observed differences in bulk sulfur isotopic composition of the two Sheepbed samples. First, although smectites observed at Sheepbed are thought to be authigenic, there are differences in interlayer spacing between JK and CB. In particular, the smectite at JK is collapsed to a basal spacing of 10 Å, whereas the smectite at CB is only partly collapsed and mostly expanded to 13.2 Å. This

expanded structure may be explained as partial intercalation by metal-hydroxyl groups[52]. The CB sample was located in close proximity to mudstone exhibiting early diagenetic Mg-rich raised ridges. The fluids involved in forming these ridges may have contributed Mg for the partial intercalation of CB smectite by metal-hydroxyl groups, which can occur as a result of interactions with hydrothermal fluids or at lower temperature conditions through interactions with Mg-rich alkaline fluids[14]. Such alkaline fluids may have been associated with "saponitization" of Fe-forsterite that resulted in the formation of magnetite and smectite clay minerals. The presence of Fe-saponite indicates that the mudstone was not subjected to alteration temperatures above ~60-80 °C, because at higher temperatures, other phyllosilicates such as corrensite, illite or chlorite would be expected to develop[14]. Second, the JK drill hole had more small fractures and nodules filled with light-toned material than the CB drill hole. Simultaneous submillimeter-scale measurements of Ca, S and H abundances of numerous light-toned veins sampled along the traverse by the Chemistry and Camera (ChemCam) instrument show that the veins contain slightly hydrated Ca-sulfate, predominantly consistent with bassanite[15,53]. Since calcium sulfates readily alter their hydration states in response to environmental conditions, the presence of bassanite in Sheepbed veins suggests that temperatures remained below ~50 °C to form gypsum, followed by subsequent dessication[53]. Mastcam data indicate that these Ca-sulfate-bearing veins cross-cut the early diagenetic features mentioned above and are thought to result from later-stage diagenetic fluids[14]. The presence of these features not only provides important evidence for more abundant late-stage fluid interactions at JK than at CB, but also provides evidence specifically of more abundant interactions with sulfur-bearing fluids at JK that could have overprinted and/or oxidized a preexisting reduced sulfur phase originally carrying a depleted isotopic signature. Third, small differences in the amounts of

akaganeite at JK and CB could result from differences in interactions, probably localized, with low-pH fluids between the two samples. Finally, the amorphous component of JK has a higher calculated sulfur abundance than that of CB[14]. This may possibly indicate a difference in the abundance of amorphous sulfur phases or adsorbed sulfate in the two samples, resulting from differences in interactions with diagenetic fluids.

The WJ sample comprises a potassium-rich basaltic mineralogy with a large amount of the K-feldspar sanidine (~21 wt.%), as well as several secondary minerals including 2:1 phyllosilicates (~10 wt %, probably collapsed smectite clay minerals), abundant magnetite (~12 wt.%) and ~15% Fe-rich amorphous material that is also high in Cl and SO_3 (perhaps present in poorly ordered sulfate phases and/or adsorbed sulfur)[39]. The magnetite, amorphous material, and phyllosilicates are likely cementing agents in the WJ sandstone, formed as a result of interactions with diagenetic fluids. WJ also contains trace pyrrhotite and trace Ca-sulfates (bassanite, anhydrite)[39]. The trace pyrrhotite could have precipitated from or been altered by the cementing fluids described above, which likely contained an isotopically enriched sulfur component. These fluids could also be responsible for the sulfur-rich nature of the amorphous component of the cement. The Ca-sulfates are likely present in WJ as a result of the late-stage diagenetic processes that have resulted in Ca-sulfate veins observed near WJ (and generally present throughout the rover's traverse), although these veins were not specifically observed within the WJ drill hole[39]. As at Sheepbed, the presence of these veins is also consistent with interactions with another generation of diagenetic fluids that could have overprinted or oxidized any preexisting sulfide.

The CH, MJ, TP, BK and OU samples were drilled from finely laminated lacustrine mudstone of the Murray formation. CH contains basaltic minerals (plagioclase, several pyroxenes, minor forsterite), poorly crystalline 10 Å phyllosilicates (~ 8 wt.%), hematite and magnetite, minor

jarosite (~1 wt %), and significant sulfur-rich amorphous material, modeled as a combination of a high-Si amorphous component and other phases, including basaltic glass and ferrihydrite. MJ has mineralogical composition generally similar to that of CH, but with more abundant jarosite (~3 wt.%) and lesser pyroxenes, hematite, and phyllosilicates. In comparison, TP has cristobalite, more abundant magnetite, only minor hematite, no phyllosilicates, and jarosite abundances more similar to CH (~1 wt.%)[54]. The BK sample contains a larger abundance of amorphous material than CH, MJ and TP, enriched in SO_3 and more enriched in SiO_2 than all previous samples. It has no mafic basaltic minerals, phyllosilicates, hematite, or jarosite, but contains magnetite, cristobalite, and significant tridymite (detected for the first time on Mars, present at ~17 wt.%)[41,54]. These mineral trends may indicate changes in the pH and redox characteristics of lake waters, as well as some differences in sediment source (e.g., a more silicic sediment source for BK), through time[54,55]. Another important feature of these samples is that the amounts of key trace elements, such as Zn and Ni, decrease with increase in elevation (from CH to BK). A major hypothesis is that these trends derive from mobilization of these elements in acidic diagenetic fluids. Provided that these fluids were sulfur-bearing, for example because sulfuric acid was the source of acidity, these trace elements could precipitate as sulfate minerals; in fact, there is evidence of Ni-, Mg-, and S-rich diagenetic features near MJ[54,56,57]. Fe-oxides can provide adsorptive surfaces for these elements[54] as well as SO_4 anions (e.g.,[58,59]). The OU sample was drilled very recently and the detailed mineralogy and chemistry data are still being interpreted. Preliminary analyses suggest a composition broadly similar to that of CH, but with the highest abundance of hematite observed in any sample to date[40]. Unlike CH and MJ, the OU sample shows no clear evidence for crystalline jarosite but does contain a substantial amount of Ca-sulfate, including anhydrite as well as the first gypsum detected within the Murray formation[40].

The BS and GH samples were drilled from outside (BS, comparatively unaltered) and inside (GH, altered BS material) a light-toned, altered fracture zone in the Stimson formation eolian sandstone. The BS sample has a generally basaltic composition, very similar to the basaltic fines sampled by Curiosity at the Rocknest eolian bedform[60], except for more abundant iron oxides (magnetite and hematite) and an absence of olivine in BS[29]. These differences could result from isochemical aqueous alteration of the original olivine and formation of the iron oxides that may now be a cementing agent in the sandstone[29]. These alteration fluids may have also precipitated or altered/oxidized preexisting sulfur phases in BS that evolve SO_2 in SAM analyses. The GH sample exhibits large amorphous silica enrichment compared to BS, offset by reduction in basaltic minerals (plagioclase and pyroxene). GH also contains substantially greater sulfur concentration and Ca-sulfate abundances (~2 wt.% bassanite and 7 wt.% anhydrite) than BS[29]. No crystalline sulfates other than these Ca-sulfates were detected by CheMin x-ray diffraction[29]. After accounting for the Ca-sulfate abundances, there is still a significant amount of sulfur remaining, based on APXS observations. Consideration of available cations detected in GH suggests that significant Fe-sulfates, and probably also mixed-cation sulfates, are likely present as components of the ~50 wt.% x-ray amorphous material in the sample[29]. The GH sample also shows elemental composition changes compared to BS. Several differences in mineralogy and chemistry between GH and BS are consistent with interactions with diagenetic fluids, likely several episodes of such interactions, and it is possible that one or more of these episodes involved acidic and/or hydrothermal solutions[29]. These fluid interactions clearly affected sulfur abundances and mineralogy near the fracture zones, and it seems likely that they also affected the isotopic compositions of sulfur-bearing phases within the samples.

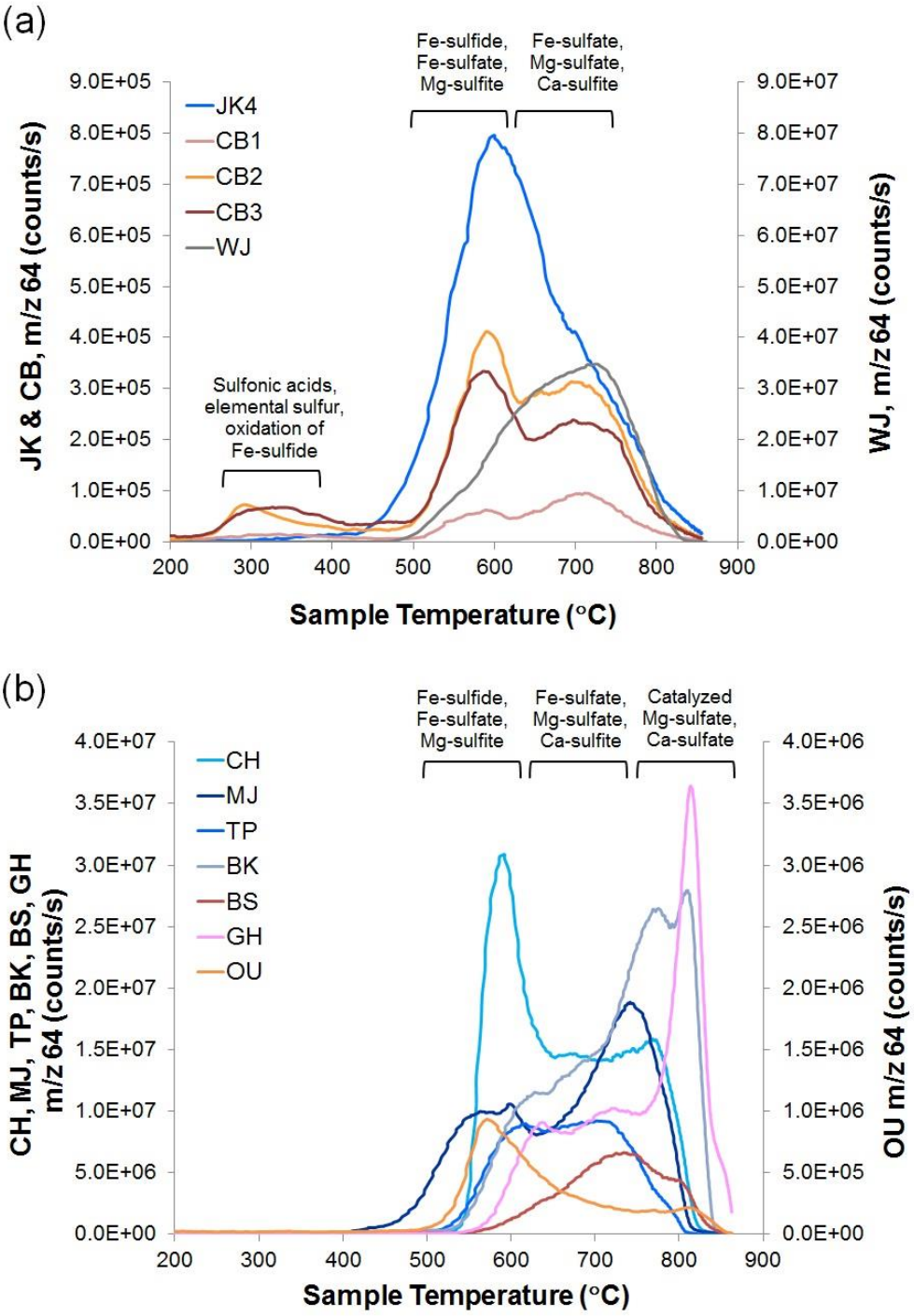

Figure S1. EGA profiles for SO_2 released from samples of (a) Bradbury Group and (b) Mount Sharp Group samples. Figure shows *m/z* 64 as a function of sample temperature. For samples in which *m/z* 64 saturated the detector, the *m/z* trace shown is estimated from *m/z* 66 to allow visual comparison of SO_2 abundances among experiments. Note different scales of y-axes.

Evaluation of equilibrium fractionation mechanisms

Fig. S2 (after ref. 36) shows the equilibrium sulfur isotopic fractionation expected between aqueous sulfate/sulfide, sulfite/sulfide, and total bisulfite/sulfide based on theoretical calculations[16]. Annotated across the top frame are the approximate times required to reach 90% sulfate/sulfide equilibrium at several different temperatures with pH ~4-7 and 0.01 mol total S/kg H_2O[35], a reasonable estimate for Gale crater fluids[17]. The range of fractionation estimated for Gale crater samples is depicted by the shaded region. Although the figure indicates that it is possible to achieve the full range of $\delta^{34}S$ (i.e., $\Delta^{34}S$ of 60-80‰) observed by SAM through equilibrium isotopic fractionation between sulfate and sulfide at temperatures of 50-75 °C, kinetic inhibition of this abiotic process at low temperatures argues against its operation within the lakebed sediments as a viable explanation for the full range of isotopic signatures observed.

Sulfur speciation during volcanic outgassing

The SO_2/H_2S ratio of Martian volcanic gases remains uncertain due to its dependence on multiple factors[61]. Recent modeling work suggests that SO_2 would likely have been the primary gas released through Martian volcanic outgassing at atmospheric pressures relevant to Mars, producing an atmospheric sulfur cycle dominated by SO_2[61]. However, as the isotopic trends produced by photochemical processing of SO_2 and H_2S are generally similar, our model is not highly dependent on sulfur speciation during volcanic outgassing. Laboratory experiments have demonstrated that broadband UV photolysis of SO_2 generates elemental sulfur products carrying large enrichments in ^{34}S, while producing simultaneous depletions of a few per mil in the residual SO_2 reservoir[20]. Similar behavior has been observed in products of H_2S photolysis

experiments[21], suggesting that elemental sulfur produced from photolytic products of either gas would be enriched in ^{34}S.

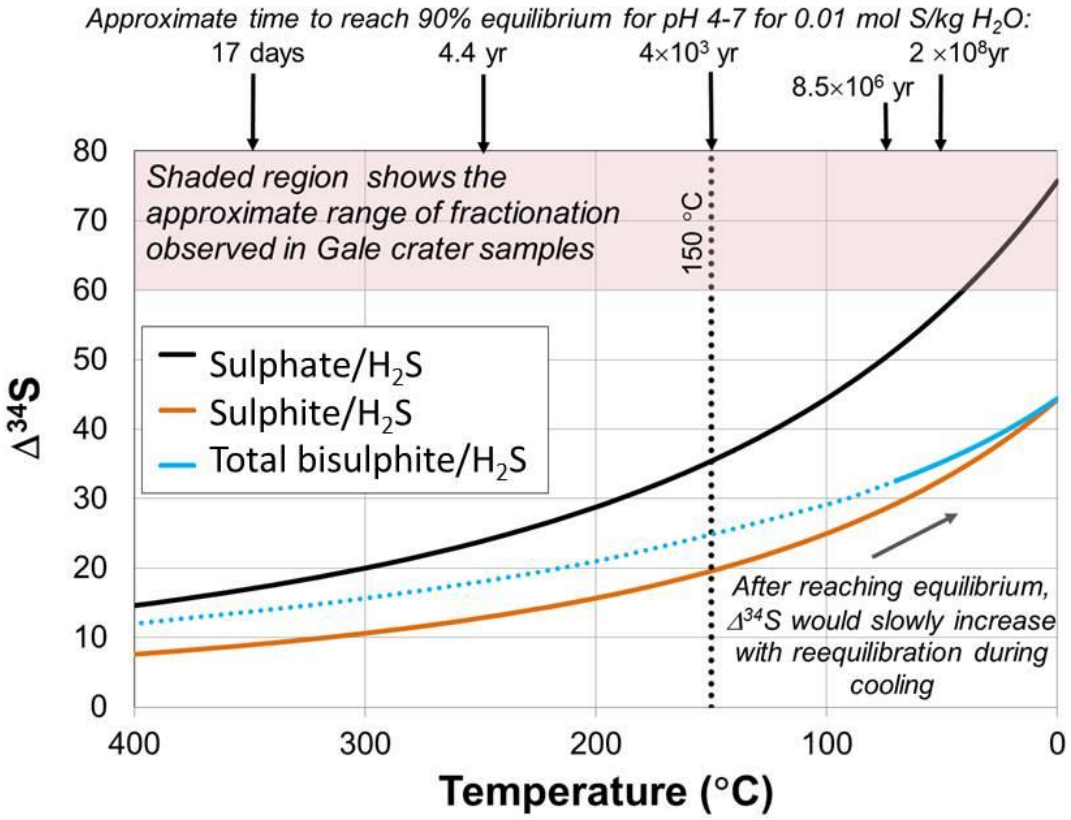

Figure S2. Theoretically calculated equilibrium sulfur isotopic fractionation between sulfate/sulfide, sulfite/sulfide, and total bisulfite/sulfide, where sulfide is modeled as H_2S and, e.g., $\Delta^{34}S = \delta^{34}S_{sulfate} - \delta^{34}S_{sulfide}$[16]. Bisulfite has two isomers, with H bonded either to sulfur or oxygen. The bisulfite/sulfide curve shown represents the net fractionation between sulfide and both bisulfite isomers; solid line indicates theoretical values using empirical isomer quotients (0-70 °C and 1 *m* ionic strength[33,34], and dotted line indicates extrapolation for temperatures > 70 °C[16]. Times required to achieve 90% equilibrium between sulfate/sulfide for pH ~4-7 and total sulfur concentration of 0.01 mol S/kg H_2O at several temperatures are annotated across top of frame[35,36]. The shaded region shows the approximate range of $\delta^{34}S$ observed in Gale crater samples reported here. Neither sulfite/sulfide nor bisulfite/sulfide equilibrium offers a means to achieve the observed fractionation. Figure modeled after ref. 36.

Curiosity Results in the Context of Sulfur Mass-Independent Fractionation

Although the SAM instrument is unable to measure isotope ratios involving the least-abundant sulfur isotopes ^{33}S and ^{36}S, as discussed in the Methods section below, sulfur mass-independent fractionation (S-MIF) is central to the isotope systematics of sulfur photochemistry, and pertinent results from analyses of Martian meteorites[6-8,11] were considered during formulation of the hypothetical model presented here. S-MIF is characterized by non-zero values of $\Delta^{33}S$ and/or $\Delta^{36}S$ (see reference 6 for the definition of these terms) and is produced by a small number of processes that fractionate sulfur isotopes in a manner not simply proportional to their masses. Laboratory gas-phase photochemistry experiments[7,20,21,62-64] and *ab initio* modeling of SO_2 UV absorption cross-sections[20,65,66] have shown that the relationship between $\Delta^{33}S$ and $\Delta^{36}S$ for a given S-MIF signature is diagnostic of the production mechanism. The continuity of the relationship between $\Delta^{33}S$ and $\Delta^{36}S$ throughout the ~4-billion-year period recorded by Martian meteorites argues for a consistent sulfur isotopic fractionation mechanism over much of Mars' history[6]. Models suggest that largely due to the water content of Martian magmas, sulfur would have been outgassed predominantly as SO_2 rather than H_2S or elemental sulfur [61,67], and that more reduced forms of sulfur would have been readily oxidized to SO_2 in the atmosphere[27]. This evidence points to SO_2 photochemistry as the most likely source for Martian S-MIF signatures[6], and by extension, implicates atmospheric reactions involving SO_2 as the probable source of $\delta^{34}S$ enrichments observed by Curiosity. Although isotopic anomalies preserved in the terrestrial record have also been dominated by SO_2 photochemistry, comparison of S-MIF signatures in Martian meteorites[6-8] with those in terrestrial samples from the Archean[68] and modern stratospheric aerosols[23,69,70] indicates that the atmosphere of Mars was dominated by a different photochemical mechanism than that prevalent on Earth[6]. In conjunction with ongoing laboratory

photochemistry investigations, this finding ultimately imposes constraints on the composition of the Martian atmosphere[6].

Alternative Fractionation Mechanisms

Although we propose that equilibrium isotopic fractionation between reduced and oxidized sulfur in aqueous conditions is most likely responsible for producing the depleted isotopic signature at CB and OU, we cannot rule out fractionation by other mechanisms for which there is currently no definitive supporting evidence. These include atmospheric chemistry, exotic sulfur chemistry, and biology.

Studies of sulfate in terrestrial volcanic ash have shown that gas-phase oxidation of SO_2 can also produce large fractionations in sulfur isotopes through multiple pathways[22,23,70]. Heterogeneous chemistry occurring in atmospheric clouds or in SO_2 and H_2O adsorbed on dust or ash particles[24,22] could produce H_2SO_4 enriched in ^{34}S by ~10‰ compared to the initial SO_2[26]. Homogeneous oxidation of SO_2 by reaction with OH radicals involves a large inverse kinetic isotope effect that also favors incorporation of ^{34}S in oxidized products[22,25]. These oxidative processes could generate fractionations of tens of per mil in the resulting sulfate aerosols. Assuming minimal isotopic fractionation during SO_2 outgassing[71], initial sulfate products would be characterized by significantly positive $\delta^{34}S$. Depending on the lifetime of SO_2 in the atmosphere following volcanic episodes and the relative rates of relevant reactions, Rayleigh distillation effects could then drive a progressive trend toward less-positive and eventually even negative values of $\delta^{34}S$ as the atmospheric SO_2 reservoir was depleted. Such isotopic trends have been observed in ash deposits following major volcanic eruptions on Earth, on time scales of several hundred days[25]. However, if all atmospheric SO_2 following a Martian volcanic episode

were ultimately oxidized to sulfate, the bulk composition of the resulting sulfate reservoir deposited at the surface would bear the signature of the original outgassed SO_2. Thus preservation of fractionated isotopic signatures in products of atmospheric chemistry requires removal and sequestration of distinct products before rehomogenization can occur. This could be implemented through records of temporal trends lithified in successive layers of sediments, separate pathways for removal and preservation of sulfur species of different oxidation states from the atmosphere, geographical variations in isotopic signatures of surface sulfur deposits driven by local environmental conditions affecting atmospheric removal processes or the combined effects of distillation and global circulation patterns, or all of the above.

Although it is possible for Rayleigh distillation effects during atmospheric oxidation processes to generate H_2SO_4 aerosols with $\delta^{34}S$ that evolves from enriched to depleted isotopic compositions over time[25], this effect would occur concurrently with a depletion of the entire atmospheric reservoir, such that the remaining SO_2 also became gradually isotopically depleted. A similar effect could occur upon extensive photolysis of SO_2 with limited back-reaction, leading to isotopic enrichment in elemental sulfur products and isotopic depletion of residual SO_2. (Note that similar arguments would apply to photolysis of H_2S, but the following discussion is based on SO_2 alone for simplicity.) The degree to which this occurred in the Martian atmosphere would have been governed by factors pertinent to SO_2 lifetime that are difficult to constrain. However, if such an evolution of SO_2 composition had occurred with relevance to the Bradbury and Mount Sharp Group sediments, there should have been a gradual depletion in ^{34}S of SO_2 removed by rainout, which should be evident in a spread of depleted isotopic signatures among samples. Similarly, we cannot rule out ^{34}S depletion due to photochemical effects that have not yet been observed in laboratory experiments. However, the observation of depleted

isotopic signatures in only two samples combined with the prevalence of ^{34}S enrichments and lack of ^{34}S depletions in secondary sulfates of Martian meteorites[6,7,11] argues against atmospheric Rayleigh distillation or photochemical effects as a source of widespread ^{34}S depletion on Mars.

In the process of equilibrium isotopic fractionation between sulfide and sulfate, the overall rate-limiting step is the initial breakage of S-O bonds in sulfate to form a thiosulfate intermediate, while the isotopic exchange rate is controlled by disproportionation of polysulfides that react with thiosulfate[72]. Although this process is kinetically inhibited at low temperatures, we acknowledge the possibility of currently unknown catalytic effects due to other components of the samples that might overcome the kinetic barrier and allow large sulfur isotopic fractionation to proceed in the sediments. For example, one indicator of different diagenetic conditions between JK and CB is the relative abundance of akaganeite, which was detected at higher abundance in CB than JK. Akaganeite, a chlorine- and iron-bearing hydroxide mineral that can form as an alteration product of pyrrhotite, is interpreted as a possible cementing agent in the hollow nodules that are more prevalent at CB than JK[14,28]. Structural equivalents of akaganeite that contain sulfate anions in place of chloride also exist[73]. Potential isotopic effects and reaction intermediates associated with the formation akaganeite as a result of pyrrhotite alteration, with or without structural sulfate, are presently unknown.

The influence of biology on the terrestrial sulfur cycle is discussed briefly in the main text. Although we are unable at this time to fully evaluate biogenicity as a source of the observed fractionations, the following discussion describes some of the factors promoting interest in sulfur from an astrobiological perspective. Along with carbon, hydrogen, nitrogen, oxygen, and phosphorus, sulfur is an essential element for extant life on Earth. Because it can assume multiple valence states from -2 to +6, sulfur can function as an energy source in both

chemoautotrophic and photosynthetic biological pathways and as a mechanism for energy storage[74]. Through biochemical processes involving both oxidation and reduction, sulfur is cycled through all of its valence states by terrestrial organisms[75]. This cycling can produce large isotopic fractionations, which may be preserved in sedimentary rocks as a record of biological activity[75]. Sulfur metabolisms originated early in the evolution of life, with isotopic evidence for sulfate reduction dating back to ~3.47 Ga[76] and sulfide oxidation to ~3.4 Ga[77]. Ion microprobe analyses of Archean shales and carbonates have revealed variations in sulfur and carbon isotopic signatures at nanometer scales, suggesting the presence of micro-reservoirs of organic matter interpreted as biogenic[38]. The depleted sulfur isotopic signature at CB and OU raises the question of whether analogous micro-reservoirs might exist in Martian sediments.

The most prevalent isotopic evidence for sulfur metabolism records use of sulfur for energy. However, sulfur is also incorporated into organic compounds comprising biological materials. Sulfur is a component of several important biochemicals, including Coenzyme A, biotin, thiamine, and insulin[74]. Sulfur is present in two of the amino acids, methionine and cysteine, required by terrestrial organisms for protein synthesis[78], and both Fe-S and S-S bonds are important in stabilizing the 3-dimensional structure of proteins[74,79]. In addition, transition metal sulfides are capable of catalyzing reactions between organic compounds relevant to biological systems[79,80].

The prevalence of iron-sulfur proteins in all types of terrestrial life has led to hypotheses suggesting that iron sulfide may have played a role in the origin of life[81-86]. Wächtershäuser's iron-sulfur world hypothesis[81-84] proposed that oxidation of FeS to pyrite could have provided an energy source for the earliest life on Earth, and furthermore that the catalytic effects of pyrite facilitated emergence of an autocatalytic reductive citric acid cycle for primordial

chemoautotrophic carbon fixation and ultimately formation of compounds essential to metabolism. In the iron-sulfur membrane hypothesis[85,86], life arose from aggregated iron sulfide bubbles enclosing alkaline, reduced hydrothermal solution, which would have formed in proximity to ocean spreading centers. Energy would have been derived from a natural proton motive force resulting from interaction between the alkaline hydrothermal fluid and an acidic ocean via the membrane[85], which would have also catalyzed reactions among organic molecules trapped inside.

In addition to representing some of the most ancient terrestrial life, some sulfate-metabolizing microbes can utilize perchlorate, chlorate, and/or nitrate instead[87,88]. This is particularly interesting in light of the abundance of oxychlorine compounds at the Martian surface[89], as well as the detection of nitrate in samples of Gale crater[90]. Reduction of perchlorate by terrestrial microbes produces chloride that is isotopically light (by ~15‰) compared to the original perchlorate[91]. Although the depleted chlorine isotopic signatures measured in sediments of Yellowknife Bay and the Murray formation by SAM were interpreted as evidence of atmospheric processing of volcanic Cl-bearing gases[30], the observed range of $\delta^{37}Cl$ is greater than that produced by either atmospheric or biological processes on Earth.

As Earth provides our only example of known biosphere, it is natural to start with the assumption that emergence and evolution of Martian life would follow the same trajectory as terrestrial life. However, we must acknowledge the possibility that Martian microbes could have developed metabolic and protective facilities that differ from those of any microbes known on Earth, characterized by unique isotopic fingerprints.

Extended Description of Methods

SAM Evolved Gas Analyses

Samples of solid Martian materials, each with mass ~45 to ~135 mg, are analyzed through evolved gas analysis (EGA), in which drilled rocks or surface fines are loaded into quartz sample cups for insertion into one of SAM's two pyrolysis ovens. All samples presented here were passed through a 150 μm sieve before loading into the sample cups. After insertion into the oven, samples are heated to ~850 °C at a rate of 35 °C/min under 25 mb He pressure, with a model-derived flow rate of 0.8 standard cubic centimeters per minute (sccm). The bottom of each quartz cup contains a porous quartz frit, allowing the He carrier gas to sweep evolved gases from the oven efficiently. During heating, a small split of the gas is directed into the quadrupole mass spectrometer (QMS) for continuous monitoring. The QMS uses an electron impact ionization source and secondary electron multiplier detector, operated in pulse-counting mode[31]. Although the QMS mass range extends from *m/z* 2 to 535, EGA experiments typically utilize a "smart-scanning" algorithm designed to optimize dwell time at masses where signal is detected during each run[31]. All data are corrected for detector effects (see "Calibration" section below) and instrument background prior to quantitative analysis.

Volatile-bearing phases often release volatiles at temperatures characteristic of their compositions; as a result, continuous QMS monitoring of gases released as a sample is heated in the pyrolysis oven can provide information helpful in determining mineral and organic content of the sample. In particular, sulfides typically break down at lower temperatures and over narrower temperature ranges than sulfates or sulfites with the same cation. Due to the high abundance of oxidants such as water and oxychlorine compounds in these samples, sulfur released from sulfides, sulfates and sulfites appears primarily as SO_2 in SAM EGA data.

Comparison of SO_2 profiles between samples highlights differences in sulfur-bearing phases. Fig. S1(a) in the main text shows SO_2 evolved from samples of the Bradbury Group. Note that multiple aliquots of the JK and CB samples were analyzed by SAM, as indicated by the numerical suffixes appended to the sample abbreviations. Data are reported here for only the fourth aliquot of JK and the first three aliquots of CB, because other aliquots of these samples utilized higher-temperature sample loading or pre-heating protocols that may have altered the behavior of sulfur phases. Fig. S1(b) shows SO_2 evolved from samples of the Mount Sharp Group. Although we cannot identify specific minerals from EGA data, in general SO_2 peaks below 600 °C are consistent with the presence of Fe-bearing sulfides or sulfates, peaks from 600-700 °C suggest Fe-sulfates, and peaks above 700 °C likely derive from Mg- or Ca-bearing sulfates, as a results of reactions with other sample phases or gases in the oven during heating [92]. SO_2 is released from Ca-sulfite ~600-800 °C [93] and from Mg-sulfite ~500-600 °C.

Analyses of JK and CB by the Chemistry and Mineralogy (CheMin) instrument revealed ~1 wt% pyrrhotite in both samples and possible pyrite at JK[14], consistent with evolution of SO_2 < 600 °C. Fig. S1(a) also shows that CB was unique in its production of a small SO_2 peak ~300 °C. Although it is possible that this SO_2 reflects oxidation of sulfide in the oven by O_2 released from an oxychlorine phase[94], there was not a similar release from the JK sample. The JK sample released less O_2 than the CB sample, which may explain the lack of ~300 °C SO_2 peak at JK compared to CB. It is also possible, however, that this low-temperature peak at CB indicates the minor presence of another sulfur-bearing phase in the CB sample. Laboratory analyses of the Murchison meteorite (Fig. S3) produced a similar SO_2 release at ~300 °C, which we attribute to sulfonic acids present in Murchison[95]. If sulfonic acid was also responsible for the SO_2 peak ~300 °C at CB, it suggests reaction between sulfur and reduced carbon compounds either in the

mudstone or in the SAM oven. Laboratory pyrolysis of altered basalts acquired near Hawaiian fumaroles containing elemental sulfur also produced SO_2 ~300 °C[96], so elemental sulfur represents another possible source for the small low-temperature peak at CB. In either case, this low-temperature peak appears as a feature unique to CB among this sample set. The majority of SO_2 released from JK and CB reflects Fe- and Mg-bearing sulfates, Ca-sulfites, or Mg-sulfites[94].

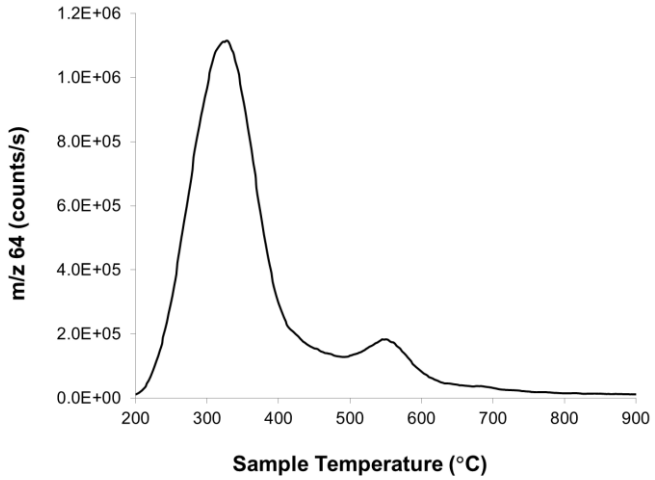

Figure S3. SO_2 profile from laboratory EGA of Murchison meteorite with the SAM breadboard. The peak ~300 °C is most likely from sulfonic acids and the peak ~550 °C is from Fe-sulfide.

Of the samples from the Kimberley formation and Mount Sharp Group, CH shows evidence for the greatest proportion of Fe-bearing sulfur compounds compared to other cations. The MJ sample also produced SO_2 between 500-600 °C consistent with Fe-sulfide, Fe-sulfate or Mg-sulfite, and ~3 wt% of the Fe-sulfate mineral jarosite was detected by CheMin in this sample[54]. SO_2 released from the remaining samples suggests varying proportions of Fe- Mg- and Ca-bearing sulfates or sulfites. This interpretation is supported by detection of anhydrite and bassanite or gypsum in diagenetic veins and filled nodules and indications from CheMin and the Alpha Particle X-ray Spectrometer (APXS) data that sulfate is a likely component of the amorphous material prevalent in all of these samples[14,15,29,97].

Sulfur Isotope Ratios

The sulfur isotopic composition is nominally calculated from SO_2 produced by thermal degradation and/or oxidation of sulfur-bearing compounds present in the samples. Sulfur isotope ratios are reported with respect to the Vienna Cañon Diablo Troilite (V-CDT) reference[32] in delta notation, where

$$\delta^{34}S = 1000 \times [(^{34}S/^{32}S)_{sample}/(^{34}S/^{32}S)_{V\text{-}CDT} - 1]. \quad (1)$$

Isotope ratios are nominally computed from the ratios of integrated peak areas for *m/z* 64 and 66 (sometimes labeled "m64" and "m66" here for simplicity), although the average of ratios of the signal at these isotopologues over the region of interest yields nearly identical results (Fig. S4).

The QMS has mass resolution of unity, requiring corrections for isobaric interferences due to oxygen isotopes. A correction algorithm was derived using an approach similar to that of[98-100], yielding the following expression:

$$^{34}R = m66/m64 - 2\times{}^{18}R - 2\times{}^{17}R\times{}^{33}R - {}^{17}R^2, \quad (2)$$

where $^{34}R = {}^{34}S/{}^{32}S$, $^{33}R = {}^{33}S/{}^{32}S$, $^{18}R = {}^{18}O/{}^{16}O$, and $^{17}R = {}^{17}O/{}^{16}O$. The signal-to-noise ratio at *m/z* 65 is too low to obtain accurate measurements of ^{33}R (and by extension, $\delta^{33}S$ and $\Delta^{33}S$) from SAM data. A study examining the sensitivity of ^{34}R calculations to the value of ^{33}R applied in

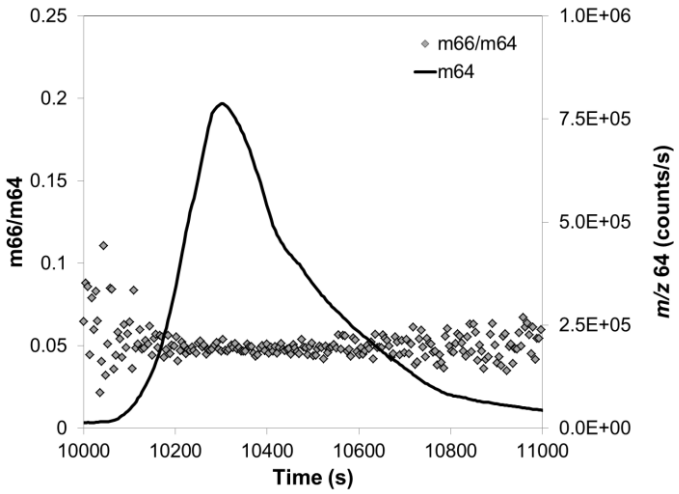

Figure S4. Example of data used to compute sulfur isotope ratios, from the John Klein (JK4) sample. The isotopic composition is calculated from the ratio of peak areas at *m/z* 64 and 66 in the range where the m66/m64 ratio is stable, near peak maximum. Uncertainties in the resulting isotopic composition are based on the variation in m66/m64 ratios in this range. See text for details.

equation (2) was performed. Three approaches were investigated for ^{33}R corrections. The nominal approach applied the value of ^{33}R computed from SAM data. The second was based on an assumption of mass-dependent fractionation in sulfur isotopes, such that $\Delta^{33}S = 0$ in the relationship

$$\Delta^{33}S = \delta^{33}S - 1000 \times [(1 + \delta^{34}S/1000)^{0.515} - 1], \quad (3)$$

with $\delta^{34}S$ and $\delta^{33}S$ calculated iteratively. In the third approach, ^{33}R was assumed to equal $^{33}S/^{32}S$ of the V-CDT reference [32]. The difference in ^{34}R obtained with these three approaches was found to be negligible, so applying corrections using ^{33}R calculated from SAM data was retained as the nominal procedure. Corrections for oxygen interferences for Mars data are based on assumptions that $\delta^{18}O = 50‰$ (current atmospheric composition)[101,102] and $\Delta^{17}O = 0.32‰$ (average for

Martian silicates)[103]. Note that the sulfur isotope calculations are not highly sensitive to assumptions concerning the oxygen isotopic composition, such that a change of 10‰ in assumed $\delta^{18}O$ produces ~1‰ change in $\delta^{34}S$. No other species with significant interferences at *m/z* 64 and 66 have been detected in SAM data.

Some samples processed by SAM contain sufficient sulfur that the evolved SO_2 saturates the detector at *m/z* 64. These cases require modifications in the calculation of sulfur isotope ratios. If the shape of the SO_2 peak is such that a stable ratio between *m/z* 64 and 66 is observed either before or after saturation occurs, it may be possible to calculate $\delta^{34}S$ from this portion of the peak. Another option is to utilize the SO fragments at *m/z* 48 and 50, using an algorithm derived in the same manner as that described previously for *m/z* 64 and 66:

$$^{34}R = m50/m48 - {}^{18}R - {}^{17}R \times {}^{33}R, \quad (4)$$

where terms and assumptions are defined as given above for equation (2). Reactions of the derivatization reagent *N*-methyl-*N*-(tert-butyldimethylsilyl)-trifluoroacetamide (MTBSTFA)[89] with Martian samples produce three compounds observed in SAM data with ionization fragments at *m/z* 50 (Fig. S5). The first compound, trifluoroacetamide, occurs at such low abundance that it may be ignored in sulfur isotope calculations. Effects of the remaining two compounds, chloromethane and methylpropene, on calculations of $\delta^{34}S$ are also minimal because they are observed in EGA data at low temperature and are generally absent by the time SO_2 starts to evolve. However, an effort is made to correct for these compounds for optimal accuracy. Modeled contributions from methylpropene are based on the behavior of *m/z* 41 and the approximate ratio of methylpropene fragments at *m/z* 50 and 41 from the National Institute of

Standards and Technology (NIST) mass spectral database. Besides *m/z* 50, the other significant fragments of chloromethane at *m/z* 49 and 52 are also isotopologues of SO, and the fragment at *m/z* 15 is dominated by nitrogen compounds[90]. For this reason, correction for the chloromethane tail at *m/z* 50 is derived either by fitting an exponential function to the fall of the chloromethane peak versus time and subtracting this from the *m/z* 50 peak due to SO or, if insufficient data are available for a reliable curve fit, by modeling the tail based on the assumption of a symmetrical chloromethane peak. Note that the abundance of SO is so large compared to chloromethane at the temperature range of interest that the correction for chloromethane is generally within the precision of the sulfur isotope calculations. When using *m/z* 48 and 50 to calculate ^{34}R, ^{33}R corrections are applied based on V-CDT composition to avoid errors due to interferences of these chlorinated compounds with SO at *m/z* 49.

For comparison of these methods, we report data for three experiments for which it was possible to calculate $\delta^{34}S$ from both SO_2 and SO fragments. The $\delta^{34}S$ of 20 ± 7‰ calculated for WJ was identical with these two methods. The second peak of BK yielded $\delta^{34}S$ of 25 ± 6‰ from SO fragments and 24 ± 9‰ from SO_2, while the second peak of BS yielded $\delta^{34}S$ of 25 ± 7‰ from SO fragments and 28 ± 6‰ from SO_2.

The baseline uncertainty for a given isotope ratio measurement is taken as the standard error of the mean (s.e.m.) for ratios of m66/m64 or m50/m48 across the portion of the peak used for isotope calculations. A possible additional source of error is background modeling. SO_2 evolved during a SAM EGA experiment typically displays an extended region of nearly constant signal during the early portion of the run, before the main SO_2 release occurs. The background is usually taken as a constant value corresponding to this average signal level. Additional background models, such as the signal level at the end of the EGA portion of the experiment or

an exponential trend to the baseline if it is obviously changing throughout the run, are also investigated to assess the robustness of the nominal background model. If this assessment indicates a sensitivity of the sulfur isotopic composition to background modeling that is outside the precision suggested by the s.e.m. of m66/m64 or m50/m48, the reported uncertainty is augmented accordingly. None of the experiments reported here required this adjustment. A final source of uncertainty derives from the assumptions regarding oxygen isotopic composition. The sensitivity of $\delta^{34}S$ to these parameters has already been discussed. An additional uncertainty in $\delta^{34}S$ of ±5‰ is factored into the reported errors to account for the assumed oxygen composition.

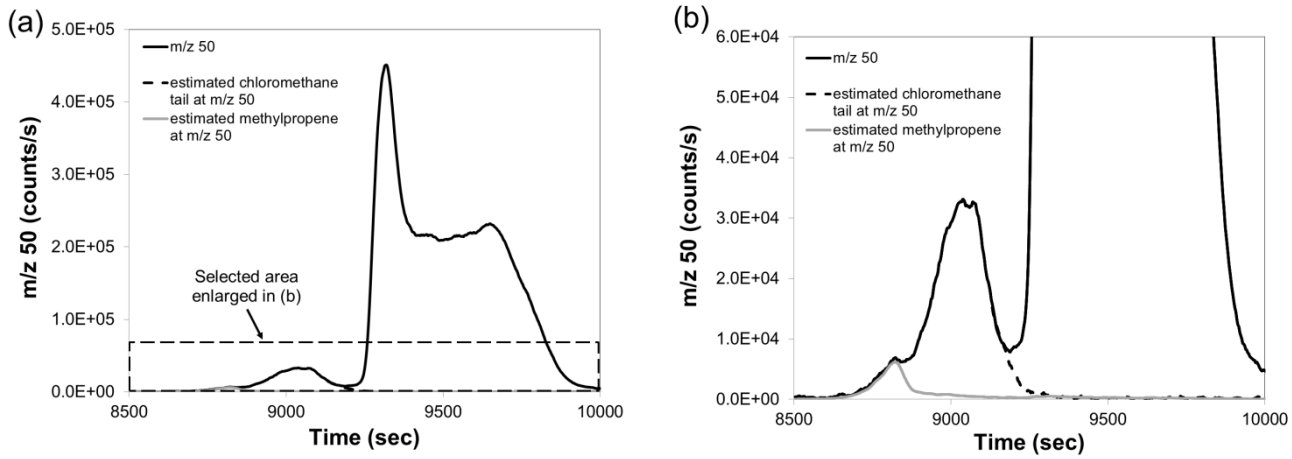

Figure S5. Illustration of MTBSTFA reaction products with fragments at *m/z* 50, which create minor isobaric interferences with SO fragments of SO_2. Effects on computation of sulfur isotopic composition from SO fragments are minimal due to depletion of MTBSTFA products prior to evolution of SO_2. Data from Confidence Hills (CH) sample are shown.

Uncertainties in Sulfur Isotopic Measurements

The two primary aspects of uncertainties in isotopic analyses are accuracy and precision. The accuracy of SAM measurements of $\delta^{34}S$ is addressed in the section discussing calibration below. Repeated analyses of standards with the SAM flight model and breadboard instruments

indicate no significant bias in measurements of sulfur isotope ratios. The precision in a given SAM measurement of $\delta^{34}S$ is dominated by counting statistics due to the magnitude of SO_2 release. As seen in Table S1, the uncertainties for individual measurements of CB aliquots were substantially larger than those of most other samples, reflecting the lower abundance of SO_2 released from CB. However, the overall uncertainty in results from CB was reduced by performing multiple analyses of the same sample from the drill. This is reflected in the uncertainty on the weighted mean for three analyses of CB shown in Table S1, which brings the confidence in measurements of CB close in line with those of the other sampling sites. As demonstrated in Fig. S6 and discussed in the section about SAM calibration below, both laboratory experiments with pyrite and SAM flight model results from Mars demonstrate no bias in $\delta^{34}S$ due to sample size.

Another factor potentially contributing to the variations in $\delta^{34}S$ observed at CB is the possibility that multiple mineral phases of different isotopic compositions contributed to each peak. For example, the SO_2 of CB Peak 1 could include contributions from hydrothermal Fe-sulfide with highly depleted composition, igneous Fe-sulfide with $\delta^{34}S$ near zero, and Fe-sulfate with enriched composition. The potential effects of such a mixture of phases are magnified at CB by the relatively low-abundance SO_2 releases. Although the relevance of this factor at CB is obvious given the repeated analyses that were performed there, it is of interest to all samples at related to data interpretation. Because it is not possible to deconvolve the contributions from multiple phases to a given SO_2 peak, we formulated our hypothesis based on the assumption that a specific peak is dominated by a single phase, with origin (e.g., atmospheric vs. hydrothermal) suggested by the degree of isotopic enrichment or depletion. However, we acknowledge that each SO_2 peak may reflect contributions from multiple components.

Calibration

Pre-launch calibration was performed on all components of the SAM suite before delivery to the Jet Propulsion Laboratory for integration with Curiosity. QMS tuning and derivation of detector correction functions, which must be applied to all SAM data prior to quantitative analyses, are described in detail by[31,104]. Pre-flight calibration to facilitate sulfur analysis was performed through EGA experiments with $FeSO_4 \cdot 4H_2O$ (Sigma-Aldrich, product #F8048, batch #048K0680). The mass of sulfate used in these experiments was sufficiently large that the SO_2 peak saturated the QMS detector at maximum count rate. For this reason, isotopic measurements were derived from data acquired before and after saturation, given in Table S2. Ratios acquired before and after saturation were weighted by their uncertainties to compute an average for each run, as shown in the table. The uncertainty on the weighted mean for all experiments, located in the lower right cell of Table S2, is shown with the associated uncertainty on the mean. Note that the standard deviation of the weighted mean values for these five experiments is ±5.5‰.

Additional calibration work was performed using laboratory test stands at NASA Goddard Space Flight Center (GSFC) in Greenbelt, MD. Calibrants for laboratory work included the $FeSO_4 \cdot 4H_2O$ described above, kieserite (ESTA® Kieserite, K+S Kali GmbH), and $CaSO_4$ (Acros). Ground truth for the sulfur isotopic composition of sulfate calibrants was determined at the Stable Isotope Laboratory of the University of Maryland Geology Department using well-established protocols.

For measurement of the $FeSO_4 \cdot 4H_2O$ composition, each powdered sample was placed in a boiling flask with 25 mL of a reduction solution prepared from 12 N hydrochloric acid, 48% hydriodic acid, and 50% hypophosphorus acid ("Thode solution")[105,106]. The flask was then assembled with a water-cooled condenser, a bubbler filled with Milli-Q water, and a sulfide trap

containing an acidic $AgNO_3$ solution into a distillation apparatus similar to that described by[8,107]. The apparatus utilized PTFE sleeves on all ground glass joints. After assembly, the apparatus was checked for leaks and purged with N_2 for at least 10 minutes. The solution was then heated to ~85 °C under N_2 flow. During the following 4.5 hours, sulfate in the sample reacted to form H_2S, which was captured in the sulfide trap as Ag_2S. Upon completion of the reduction, the Ag_2S in the sulfide trap was cleaned with Milli-Q water and 1 M NH_4OH solution, then dried.

Silver sulfide obtained from reduction of $FeSO_4 \cdot 4H_2O$ was converted to SF_6 by reaction with 250 μmoles of F_2 gas in a nickel reaction vessel at 250 °C for 8 hours. The SF_6 was subsequently condensed from the residual F_2 into a trap cooled with liquid N_2. Excess F_2 was passivated by reaction with KBr salt. The liquid N_2 coolant on the trap was replaced with ethanol slush at -115 °C to allow distillation of the SF_6 from the trap into the liquid-N_2-cooled injection loop of a gas chromatograph (GC). The SF_6 was purified by a 1/8-inch diameter, 6-foot long Molecular Sieve 5A GC column, followed by a 1/8-inch diameter, 12-foot long Haysep-Q™ GC column. Both columns were held at 50 °C, with helium carrier gas flow rate of 20 mL/min. After its elution from the GC, the SF_6 was captured in spiral glass traps cooled with liquid N_2, then transferred to the bellows of a Thermofinnigan MAT 253 dual-inlet gas source mass spectrometer. The sulfur isotopic composition of the SF_6 is measured by monitoring SF_5^+ ion beams at *m/z* 127, 128, 129, and 131.

Samples of kieserite and $CaSO_4$ calibrants were combusted to SO_2 using a Eurovector elemental analyzer in-line with an Isoprime isotope ratio mass spectrometer (IRMS). Each sample was loaded into a tin sample cup and mixed with V_2O_5 to enhance combustion to SO_2. The tin cup was dropped with a pulsed O_2 surge of 12 mL into a catalytic combustion furnace operating at 1030 °C. The frosted quartz reaction tube was packed with high-purity copper wire

to ensure quantitative oxidation and resorption of O_2. Water was removed from combustion products with a 10-cm $Mg(ClO_4)_2$ column, then SO_2 was separated from other gases with a 0.8-m PTFE GC column packed with Porapak 50-80 mesh, heated to 115 °C. The effluent from the elemental analyzer was introduced with He carrier gas to the IRMS through a SGE splitter valve. Isotope ratios of reference and sample peaks were determined by monitoring ion beams at *m/z* 64 and 66.

The ground-truth sulfur isotopic composition of each calibrant is given in Table S3. Comparison of the average $\delta^{34}S$ measured by SAM for the $FeSO_4 \cdot 4H_2O$ standard (Table S2) with that obtained via bulk sulfur extraction and fluorination techniques (Table S3) indicates that any SAM instrumental mass fractionation between *m/z* 64 and 66 is within the measurement precision. Thus no correction for mass fractionation is applied during the calculation of sulfur isotope ratios from SAM data.

Effects of perchlorate on $\delta^{34}S$

The oxychlorine compounds, interpreted as predominantly perchlorate[89], in all Martian samples analyzed produces HCl at temperatures that overlap with those of SO_2 evolution[108]. This is beneficial in that it may allow detection of more refractory Mg- and Ca-sulfates that would otherwise degrade at temperatures above SAM's operating range[92]. However, laboratory experiments with calibrants and analog samples were conducted to test whether reactions between HCl and SO_2 would fractionate sulfur isotopes. Experiments were conducted using the SAM breadboard test stand at NASA GSFC. This system utilizes the SAM prototype QMS identical to that of the flight model, with a laboratory version of the pyrolysis oven that allows

manual loading of samples. Experiments used the same helium carrier gas pressure and temperature ramp as those in runs on Mars. Results are shown in Table S4.

The first set of experiments examined possible fractionation effects in SO_2 produced by reaction between perchlorate and kieserite. ESTA kieserite calibrant was mixed with FS-120 fused silica doped with 1 wt% Mg-perchlorate. Average results for three experiments gave $\delta^{34}S$ of 8.9 ± 11.7‰, compared to the actual value of 10.14 ± 0.11‰.

Another set of experiments was performed with mixtures of perchlorate and a terrestrial analogue sample dating to the Archean. These experiments utilized a sulfur extract, predominantly pyrite, from the Jeerinah formation (WRL1 drill core) of the Hamersley Basin in Western Australia[37], mixed with a martian sediment analogue. This sample was selected because it would readily release SO_2 within the SAM operating range and because it provided a good analogue to the sulfide component of the Cumberland (CB) sample. A set of eight initial experiments pyrolyzed WRL1 sample either alone or mixed with JSC Mars-1 simulant[109] that had been baked overnight at 500 °C to eliminate organic contaminants, yielding average $\delta^{34}S$ of 3.4 ± 4.9‰, compared to the average of 3.32 ± 2.23‰ for Jeerinah formation sulfur components reported by[37]. To test effects of perchlorate, small aliquots of the WRL1 sample were mixed with the JSC Mars-1 simulant described above, then spiked with 1 wt% of either Ca-perchlorate or Mg-perchlorate. Nine experiments produced average $\delta^{34}S$ of 2.0 ± 7.0‰. Results are shown in Fig. S6(a), which also includes the average $\delta^{34}S$ from[37], the range of $\delta^{34}S$ measured for individual WRL1 sulfide grains measured by ion microprobe[38], and the approximate range of $\delta^{34}S$ measured by SAM in the CB3 aliquot. These experiments indicate no systematic bias in $\delta^{34}S$ due to the presence of perchlorate. The variations in $\delta^{34}S$ among breadboard experiments were of comparable magnitude to the range observed for individual grains by ion microprobe[38].

The data shown in Fig. S6(a) for Jeerinah pyrite analyzed both in isolation and combined with a Mars analogue mixture demonstrate no evidence for matrix effects, such as collisions of matrix ions with SO_2 or SO ions in the QMS source. In addition, our results indicate no evidence of SO_2 recombination reactions or isotopic fractionation within the QMS source that affect the accuracy of measured $\delta^{34}S$ within the stated precision for QMS analyses.

Fig. S6(b) demonstrates the absence of correlation between $\delta^{34}S$ measured for the Jeerinah pyrite with the QMS and SO_2 signal intensity, shown as the maximum signal at *m/z* 66 during the EGA peak. This figure also includes analogous data for individual peaks of the CB and OU samples that revealed negative values of $\delta^{34}S$ as measured by SAM on Mars and that we attribute to sulfides. Fig. S6(c) is an expanded view of the previous figure for the range of *m/z* 66 signal up to 5.0e+04 counts/s, which encompasses the range of peak intensities at CB and OU. The SO_2 peaks observed for samples on Mars, which typically contain a few to several wt% sulfur, are understandably much smaller than those obtained in the laboratory by processing pure mineral phases. However, the plots in Fig. S6 demonstrate no systematic bias in $\delta^{34}S$ due to variations in peak intensity for Jeerinah pyrite samples, including those within the range of SO_2 peak size observed at CB and OU. Furthermore, Fig. S6(c) suggests no signal intensity bias between individual peaks analyzed at CB and OU on Mars, despite the fact that the isotopically depleted OU peak that we attribute to sulfide is approximately an order of magnitude larger than the peaks of the CB1 sample. These data support our interpretation that the depleted sulfur isotopic signatures measured for these peaks, and their association with sulfides, represent distinct and statistically significant variations in composition from those sulfate-derived peaks in other locations sampled by Curiosity.

A final set of experiments investigated possible isotopic fractionation during pyrolysis of perchlorate and Ca-sulfite. The isotopic composition of the sulfite was not measured independently, but experiments were performed on the SAM breadboard both with and without perchlorate for comparison of the resulting $\delta^{34}S$. The average $\delta^{34}S$ for two runs of Ca-sulfite without perchlorate was 1.2 ± 11.2‰, compared to an average of -10.2 ± 9.9‰ for two runs using a mixture of Ca-sulfite and FS-120 doped with 1 wt% Ca-perchlorate. These results overlap and do not indicate isotopic fractionation during pyrolysis of sulfite due to the presence of perchlorate.

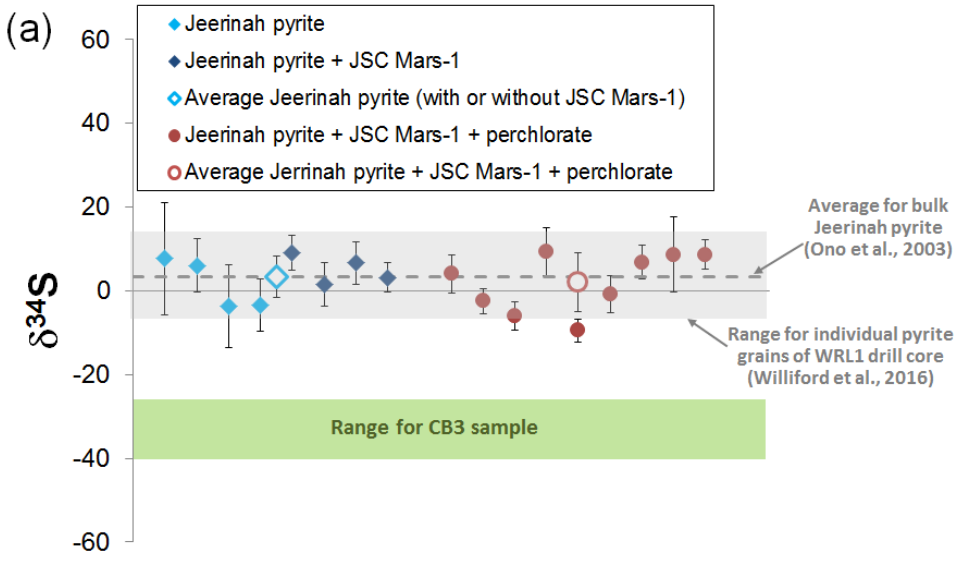

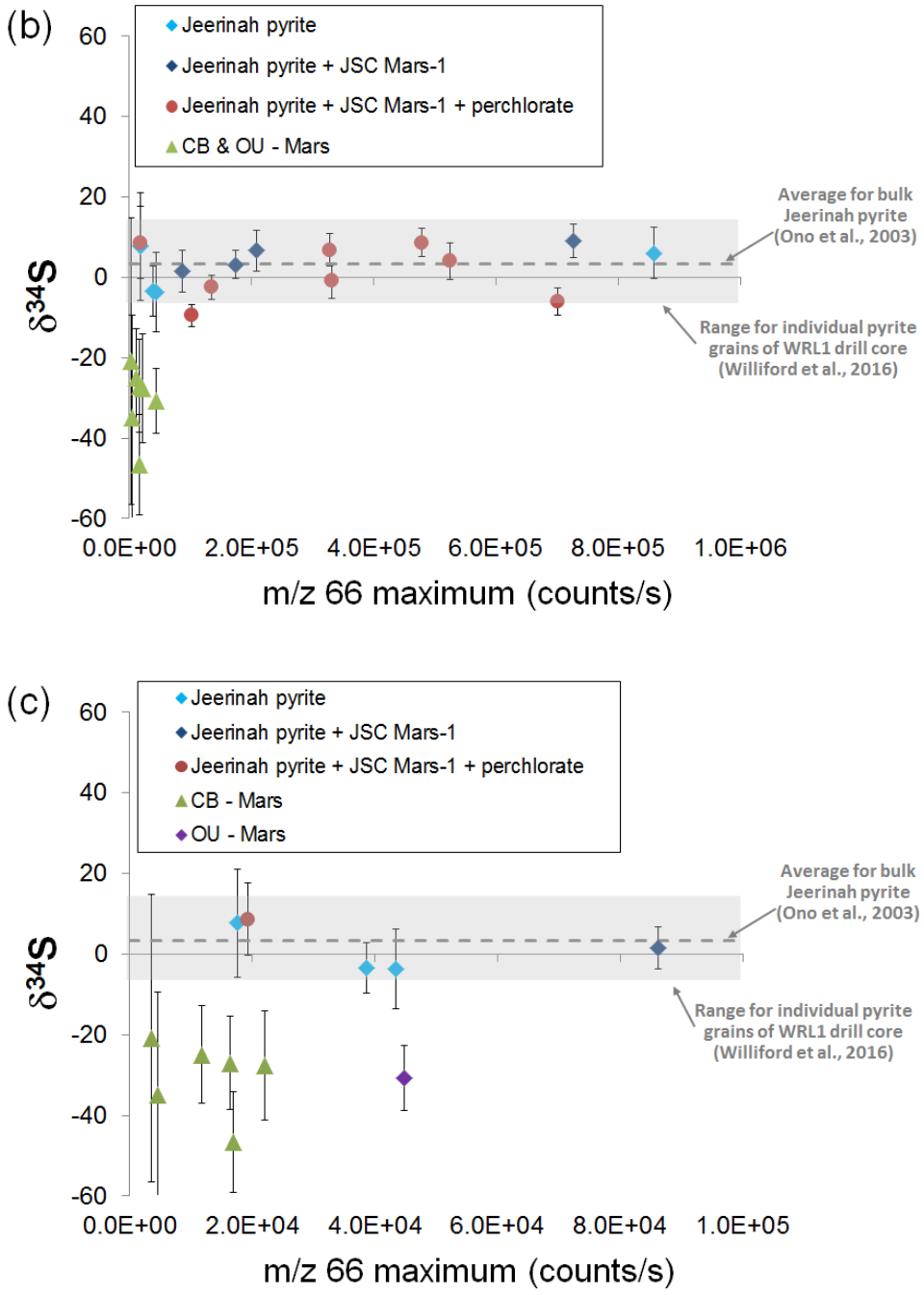

Figure S6. (a) Sulfur isotopic data ($\delta^{34}S$ vs. experiment number) for sulfur extract from the Archean Jeerinah formation as measured with the SAM breadboard, along with results reported for analyses by chemical extraction[37] and ion microprobe[38] techniques. Experiments performed with the sulfur extract in isolation or mixed with JSC Mars-1 simulant demonstrate no matrix effects on the retrieved sulfur isotopic composition. Experiments performed both with and without perchlorate demonstrate no effects on the retrieved sulfur isotopic composition due to the presence or abcence of perchlorate in the sample. (b) Jeerinah pyrite $\delta^{34}S$ vs. SO_2 signal intensity, parameterized as maximum signal at *m/z* 66 for each peak. Data for CB and OU peaks

observed on Mars and attributed to sulfides are also shown for comparison. (c) Expanded view of (b), showing data for *m/z* 66 below 5.0e+04 counts/s to highlight the range relevant to Mars samples. The plots in (b) and (c) demonstrate no bias in $\delta^{34}S$ due to sample size.

References:

33 Horner, D. A. & Connick, R. E. Equilibrium quotient for the isomerization of bisulfite ion from HSO_3- to SO_3H-. Inorg. Chem. 25, 2414-2417 (1986).

34 Littlejohn, D., Walton, S. A. & Chang, S.-G. A Raman study of the isomers and dimer of hydrogen sulfite ion. Appl. Spectrosc. 46, 848-851 (1992).

35 Ohmoto, H. & Lasaga, A. C. Kinetics of reactions between aqueous sulfates and sulfides in hydrothermal systems. Geochim. Cosmochim. Acta 46, 1727-1745 (1982).

36 Rye, R. O. A review of the stable-isotope geochemistry of sulfate minerals in selected igneous environments and related hydrothermal systems. Chem. Geol. 215, 5-36 (2005).

37 Ono, S. et al. New insights into Archean sulfur cycle from mass-independent sulfur isotope records from the Hamersley Basin, Australia. Earth Planet. Sci. Lett. 213, 15-30, (2003).

38 Williford, K. H. et al. Carbon and sulfur isotopic signatures of ancient life and environments at the microbial scale: Neoarchean shales and carbonates. Geobiology 14, 105-128 (2016).

39 Treiman, A. H. et al. Mineralogy, provenance, and diagenesis of a potassic basaltic sandstone on Mars: CheMin X-ray diffraction of the Windjana sample (Kimberley area, Gale Crater). J. Geophys. Res. Planets 121, 75-106 (2016).

40 Rampe, E. et al.Mineralogical and geochemical trends in a fluviolacustrine sequence in Gale crater, Mars. Goldschmidt Conf., Japan, 2582 (2017).

41 Morris, R. V. et al. Silicic volcanism on Mars evidenced by tridymite in high-SiO_2 sedimentary rock at Gale crater. Proc. Natl. Acad. Sci. 113, 7071-7076 (2016).

42 Thomson, B. J. et al. Constraints on the origin and evolution of the layered mound in Gale Crater, Mars using Mars Reconnaissance Orbiter data. Icarus 214, 413-432 (2011).

43 Le Deit, L. et al. Sequence of infilling events in Gale Crater, Mars: Results from morphology, stratigraphy, and mineralogy. J. Geophys. Res. 118, 2439-2473 (2013).

44 Tanaka, K. L. The stratigraphy of Mars. J. Geophys. Res. 91, E139-E158 (1986).

45 Milliken, R. E., Grotzinger, J. P. & Thomson, B. J. Paleoclimate of Mars as captured by the stratigraphic record in Gale Crater. Geophys. Res. Lett. 37, L04201 (2010).

46 Leveille, R. J. et al. Chemistry of fracture-filling raised ridges in Yellowknife Bay, Gale Crater: Window into past aqueous activity and habitability on Mars. J. Geophys. Res. Planets 119, 2398-2415 (2014).

47 Siebach, K. L. et al. Subaqueous shrinkage cracks in the Sheepbed mudstone: Implications for early fluid diagenesis, Gale crater, Mars. J. Geophys. Res. Planets 119, 1597-1613 (2014).

48 Grotzinger, J. P. et al. A habitable fluvio-lacustrine environment at Yellowknife Bay, Gale Crater, Mars. Science 343, 1242777 (2014).

49 Leveille, R. J. et al. Chemistry of fracture-filling ridges in Yellowknife Bay, Gale Crater: Window into past aqueous activity and habilitability on Mars. J. Geophys. Res. Planets 119, 2398-2415 (2014).

50 Banham, S. G. et al. Reconstruction of an ancient eolian dune field at Gale crater, Mars: Sedimentary analysis of the Stimson formation. Lunar Planet Sci. XLVII, The Woodlands, TX, 2346 (2016).

51 Morris, R. V. et al. Update on the chemical composition of crystalline, smectite, and amorphous components for Rocknest soil and John Klein and Cumberland mudstone drill fines at Gale crater, Mars. Lunar Planet. Sci. XLVI, The Woodlands, TX, 1832 (2015).

52 Bristow, T. F. et al. The origin and implications of clay minerals from Yellowknife Bay, Gale crater, Mars. Amer. Min. 100, 824-836 (2015).

53 Rapin, W. et al. Hydration state of calcium sulfates in Gale crater, Mars: Identification of bassanite veins. Earth Planet. Sci. Lett. 452, 197-205 (2016).

54 Rampe, E. et al. Mineralogy of an ancient lacustrine mudstone succession from the Murray formation, Gale crater, Mars. Earth Planet. Sci. 471, 172-185 (2017).

55 Hurowitz, J. A. Redox stratification of an ancient lake in Gale crater, Mars. Science 356, AAH6849 (2017).

56 Nachon, M. et al. Diagenetic features analyzed by ChemCam/Curiosity at Pahrump Hills, Gale crater, Mars. Lunar Planet. Sci. XLVI, The Woodlands, TX, 1832 (2015).

57 Kah, L. C. et al. Late diagenetic cements in the Murray Formation, Gale Crater, Mars: Implications for Postdepositional fluid flow. AGU Fall Mtg., San Francisco, CA, P53F-05 (2015).

58 Aylmore, L. A. G., Karim, M. & Quirk, J. P. Adsorption and desorption of sulfate ions by soil constituents. Soil Sci. 103, 10-15 (1967).

59 Rampe, E. B., Morris, R. V., Archer, P. D., Agresti, D. G. & Ming, D. W. Recognizing sulfate and phosphate complexes chemisorbed onto nanophase weathering products on Mars using in-situ and remote observations. Am. Mineral. 101, 678-689 (2016).

60 Bish, D. L. et al. X-ray diffraction results from Mars Science Laboratory: Mineralogy of Rocknest at Gale Crater. Science 341, 1238932 (2013).

61 Gaillard, F., Michalski, J., Berger, G., McLennan, S. M. & Scaillet, B. Geochemical reservoirs and timing of sulfur cycling on Mars. Space Sci. Rev. 174, 251-300 (2013).

62 Farquhar, J., Savarino, J., Airieau, S. & Thiemens, M. H. Observation of wavelength-sensitive mass-independent sulfur isotope effects during SO2 photolysis: Implications for the early atmosphere. J. Geophys. Res. 106, 32829-32839 (2001).

63 Masterson, A. L., Farquhar, J. & Wing, B. A. Sulfur mass-independent fractionation patterns in the broadband UV photolysis of sulfur dioxide: Pressure and third body effects. Earth Planet. Sci. Lett. 306, 253-260 (2011).

64 Whitehill, A. R., Jiang, B., Guo, H. & Ono, S. SO_2 photolysis as a source for sulfur mass-independent isotope signatures in stratospheric aerosols. Atmos. Chem. Phys. 15, 1843-1864 (2015).

65 Danielache, S. O., Eskebjerg, C., Johnson, M. S., Ueno, Y. & Yoshida, N. High-precision spectroscopy of ^{32}S,^{33}S, and ^{34}S sulfur dioxide: Ultraviolet absorption cross sections and isotope effects. J. Geophys. Res. 113, D17314 (2008).

66 Danielache, S. O. et al. Photoabsorption cross-section measurements of ^{32}S,^{33}S,^{34}S, and ^{36}S sulfur dioxide for the B^1B_1-X^1A_1 absorption band. J. Geophys. Res. 117, D24301 (2012).

67 Gaillard, F. & Scaillet, B. The sulfur content of volcanic gases on Mars. Earth Planet. Sci. Lett. 279, 34-43 (2009).

68 Farquhar, J., Bao, H. & Thiemens, M. Atmospheric influence of Earth's earliest sulfur cycle. Science 289, 756-758 (2000).

69 Baroni, M., Thiemens, M. H., Delmas, R. J. & Savarino, J. Mass-independent sulfur isotopic compositions in stratospheric volcanic eruptions. Science 315, 84-87 (2007).

70 Baroni, M., Savarino, J., Cole-Dai, J., Rai, V. K. & Thiemens, M. H. Anomalous sulfur isotope compositions of volcanic sulfate over the last millennium in Antarctic ice cores. J. Geophys. Res. 113, D20112 (2008).

71 de Moor, J. M., King, P. L., Sharp, Z. D. & Fischer, T. P. A model for sulfur speciation and sulfur isotope fractionation during magmatic degassing on Earth and Mars. Lunar Planet Sci. XLII, The Woodlands, TX, 1238 (2011).

72 Chu, X., Ohmoto, H. & Cole, D. R. Kinetics of sulfur isotope exchange between aqueous sulfide and thiosulfate involving intra- and intermolecular reactions at hydrothermal conditions. Chem. Geol. 211, 217-235 (2004).

73 Peretyazhko, T. S. et al. Synthesis of akaganeite in the presence of sulfate: Implications for akaganeite formation in Yellowknife Bay, Gale Crater, Mars. Geochim. Cosmochim. Acta 188, 284-296 (2016).

74 Clark, B. C. Sulfur – Fountainhead of life in the universe. Proc. Conf. on Life in the Universe. (ed J. Billingham), NASA Ames Research Center, June 19-20, 1979. MIT Press, 47 (1981).

75 Canfield, D. E. Biogeochemistry of Sulfur Isotopes. Reviews in Mineralogy 43, 607-636 (2001).

76 Shen, Y., Buick, R. & Canfield, D. E. Isotopic evidence for microbial sulfate reduction in the early Archaean era. Nature 410, 77-81 (2001).

77 Wacey, D., Saunders, M., Braiser, M. D. & Kilburn, M. R. Earliest microbially-mediated pyrite oxidation in ~3.4 billion-year-old sediments. Earth Planet. Sci. Lett. 301, 393-402 (2011).

78 McMurry, J. Organic Chemistry. 6th ed. Brooks/Cole-Thomson Learning (2004).

79 Beinert, H., Holm, R. H. & Munck, E. Iron-sulfur clusters: Nature's modular, multipurpose structures. Science 277, 653-659 (1997).

80 Cody, G. D. Transition metal sulfides and the origins of metabolism. Ann. Rev. Earth Planet. Sci. 32, 569-599 (2004).

81 Wachtershauser, G. Before enzymes and templates: Theory of surface metabolism. Microb. Rev. 52, 452-484 (1988).

82 Wachtershauser, G. Pyrite formation, the first energy source for life: A hypothesis. Syst. Appl. Microbiol. 10, 207-210 (1988).

83 Wachtershauser, G. Evolution of the first metabolic cycles. Proc. Natl. Acad. Sci. 87, 200-204 (1990).

84 Wachtershauser, G. Ground works for an evolutionary biochemistry: The iron-sulfur world. Prog. Biophys. Mol. Biol. 58, 85-201 (1992).

85 Russell, M. J., Daniel, R. M., Hall, A. J. & Sherringham, J. A. A hydrothermally precipitated catalytic iron sulfide membrane as a first step toward life. J. Mol. Evol. 39, 231-243 (1994).

86 Russell, M. J. & Hall, A. J. The emergence of life from iron monosulfide bubbles at a submarine hydrothermal redox and pH front. J. Geol. Soc. London 154, 377-402 (1997).

87 Liebensteiner, M. G., Stams, A. J. M. & Lomans, B. P. (Per)chlorate reduction at high temperature: Physiological study of Archaeoglobus fulgidus and potential implications for novel souring mitigation strategies. Int. Biodet. Biodegrad. 96, 216-222 (2014).

88 Balk, M., van Gelder, T., Weelink, S. A. & Stams, A. J. M. (Per)chlorate reduction by the thermophilic bacterium Moorella perchloratireducens sp. nov., isolated from underground gas storage. Appl. Environ. Microbiol. 74, 403-409 (2008).

89 Glavin, D. P. et al. Evidence for perchlorates and the origin of chlorinated hydrocarbons detected by SAM at the Rocknest aeolian deposit in Gale Crater. J. Geophys. Res. 119, 1-19 (2013).

90 Stern, J. C. et al. Evidence for indigenous nitrogen in sedimentary and aeolian deposits from the Curiosity rover investigations at Gale Crater, Mars. Proc. Natl. Acad. Sci. 112, 4245-4250 (2015).

91 Sturchio, N. C. et al. Oxygen and chlorine isotopic fractionation during perchlorate biodegradation: Laboratory results and implications for forensics and natural attenuation studies. Environ. Sci. Technol. 41, 2796-2802 (2007).

92 McAdam, A. C. et al. Reactions involving calcium and magnesium sulfates as potential sources of sulfur dioxide during MSL evolved gas analysis. Lunar Planet Sci. XLVII, The Woodlands, TX, 2277 (2016).

93 McAdam, A. C. et al. Sulfur-bearing phases detected by evolved gas analysis of the Rocknest aeolian deposit, Gale Crater, Mars. J. Geophys. Res. Planets 119, 373-393 (2014).

94 Ming, D. W. et al. Volatile and organic compositions of sedimentary rocks in Yellowknife Bay, Gale Crater, Mars. Science 343, 1245267 (2014).

95 Cooper, G. W. Sulfur and Hydrogen Isotope Anomalies in Meteorite Sulfonic Acids. Science 277, 1072-1074 (1997).

96 McAdam, A. et al. MSL SAM-like analyses of Hawaiian altered basaltic materials: Implications for analysis by the Mars Science Laboratory. AGU Fall Mtg., San Francisco, CA, P31A-2034 (2015).

97 McLennan, S. M. et al. Elemental geochemistry of sedimentary rocks at Yellowknife Bay, Gale Crater, Mars. Science 343, 1244734 (2014).

98 Thode, H. G., Macnamara, J. & Collins, C. B. Natural variations in the isotopic content of sulfur and their significance. Can. J. Res. 27, 361-373 (1949).

99 Craig, H. Isotopic standards for carbon and oxygen and correction for mass-spectrometric analysis of carbon dioxide. Geochim. Cosmochim. Acta 12, 133-149 (1957).

100 Coleman, M. in Handbook of Stable Isotope Analytical Techniques Vol. 1 (ed P. de Groot) Elsevier (2004).

101 Mahaffy, P. R. et al. Abundance and isotopic composition of gases in the martian atmosphere from the Curiosity rover. Science 341, 263-266 (2013).

102 Webster, C. R. et al. Isotope ratios of H, C, and O in CO_2 and H_2O of the martian atmosphere. Science 341, 260-263 (2013).

103 Franchi, I. A., Wright, I. P., Sexton, A. S. & Pillinger, C. T. The oxygen-isotopic composition of Earth and Mars. Met. Planet. Sci. 34, 657-661 (1999).

104 Franz, H. B. et al. Reevaluated martian atmospheric mixing ratios from the mass spectrometer on the Curiosity rover. Planet. Space Sci. 109-110, 154-158 (2015).

105 Mayer, B. & Krouse, H. R. Procedures for sulfur isotope abundance studies. de Groot, P. (Ed.), Handbook of Stable Isotope Analytical Techniques, Vol. 1, 538-596 (2004).

106 Thode, H. G., Monster, J. & Dunford, H. B. Sulfur isotope geochemistry. Geochim. Cosmochim. Acta 25, 159-174 (1961).

107 Forrest, J. & Newman, L. Silver-110 microgram sulfate analysis for the short time resolution of ambient levels of sulfur aerosol. Anal. Chem. 49, 1579-1584 (1977).

108 Archer, P. D., Jr. et al. Abundances and implications of volatile-bearing species from evolved gas analysis of the Rocknest aeolian deposit, Gale Crater, Mars. J. Geophys. Res. Planets 119, 237-254 (2014).

109 Allen, C. C. et al. Martian soil simulant available for scientific, educational study. Eos. Trans. 79, 405-409 (1998).